




Formation of fused aggregates under long-term microgravity conditions aboard the ISS with implications for early solar system particle aggregation

Tamara E. KOCH ^{*1}, Dominik SPAHR¹, Beverley J. TKALCEC ¹, Oliver CHRIST²,
Philomena-Theresa GENZEL¹, Miles LINDNER ¹, David MERGES¹, Fabian WILDE³,
Björn WINKLER¹, and Frank E. BRENKER^{1,4}

¹Institute of Geosciences, Goethe University Frankfurt, Altenhoferallee 1, 60438 Frankfurt am Main, Germany

²Department of Geoscience, University of Padua, Via Gradenigo 6, 35131 Padua, Italy

³Helmholtz-Zentrum Hereon, Max-Planck Strasse 1, 21502 Geesthacht, Germany

⁴Hawai'i Institute of Geophysics and Planetology, School of Ocean and Earth Science and Technology, University of Hawai'i at Mānoa, 1680 East-West Road, Honolulu, Hawaii 96822, USA

*Corresponding author. E-mail: t.koch@em.uni-frankfurt.de

(Received 20 July 2021; revision accepted 23 March 2022)

Abstract—In order to gain further insights into early solar system aggregation processes, we carried out an experiment on board the International Space Station, which allowed us to study the behavior of dust particles exposed to electric arc discharges under long-term microgravity. The experiment led to the formation of robust, elongated, fluffy aggregates, which were studied by scanning electron microscopy, electron backscatter diffraction, and synchrotron micro-computed tomography. The morphologies of these aggregates strongly resemble the typical shapes of fractal fluffy-type calcium-aluminum-rich inclusions (CAIs). We conclude that a small amount of melting could have supplied the required stability for such fractal structures to have survived transportation and aggregation to and compaction within planetesimals. Other aggregates produced in our experiment have a massy morphology and contain relict grains, likely resulting from the collision of grains with different degrees of melting, also observed in some natural CAIs. Some particles are surrounded by igneous rims, which remind in thickness and crystal orientation of Wark–Lovering rims; another aggregate shows similarities to disk-shaped CAIs. These results imply that a (flash-)heating event with subsequent aggregation could have been involved in the formation of different morphological CAI characteristics.

INTRODUCTION

The aggregation of particles in the solar nebula is generally considered the first process leading to planet formation (Blum & Wurm, 2008; Dominik et al., 2006). Refractory inclusions such as calcium-aluminum-rich inclusions (CAIs) and amoeboid olivine aggregates (AOAs) are considered to be the oldest material of our solar system (Connelly et al., 2012; Krot et al., 2009) and likely witnesses of early aggregation processes. The chemical properties of CAIs and AOAs have been intensively studied in the past with regard to their condensation origin (e.g., Connelly et al., 2012; Han & Brearley, 2015; Krot et al., 2009; Krot, Petaev, Russell, et al., 2004; Krot, Petaev, & Yurimoto, 2004; Sugiura et al., 2009). Their structural characteristics, such as morphologies, texture, and porosity, bear further

knowledge about the processes regarding the circumstances of aggregation, reheating, annealing, recrystallization, compaction, as well as solar nebula dynamics and material transportation (Komatsu et al., 2001, 2009; Rubin, 2012; Sugiura et al., 2009).

With ²⁰⁷Pb–²⁰⁶Pb ages of 4567.3 ± 0.16 Ma (Connelly et al., 2012), CAIs formed as the first solids of the solar system, close to the Sun and probably over a period of 0.3 Ma (Kita et al., 2013). The sojourn time of CAIs in their original condensation region was probably very short, about 2000 yr, until they were either drawn into the Sun or transported outward (Taillifet et al., 2014). Because several generations of CAIs have been recognized, CAI transportation to the outer regions of the disk, by a yet undefined process, must have been a frequent event (reviewed in Krot, 2019).

CAIs (especially in CV chondrites) are classified according to their mineralogy in types A, B, and C (Krot, 2019) and further characterized by morphology, texture, and microstructure. Type A CAIs occur either as spheroidal and compact CAIs (Compact Type A: CTA) that have experienced melting, or as irregularly shaped, nonmolten fluffy-type CAIs (Fluffy-type A: FTA). Type B CAIs are usually interpreted to have formed by melting and fractional crystallization (Blander & Fuchs, 1975).

Fluffy-type CAIs have very irregular, fractal structures, which resemble the structures formed from hit-and-stick collision experiments and modeling (e.g., Blum & Wurm, 2008; Blum et al., 2000). Aggregation of micrometer particles to millimeter-sized objects by surface adhesion at 1 AU was probably a fast process of 10–100 yr (Brauer et al., 2007; Charnoz & Taillifet, 2012). However, the question arises how these fragile, fractal structures could survive turbulences and transportation to the outer protoplanetary disk (PPD), chondrite aggregation, and subsequent compaction. One explanation is that FTA CAIs potentially aggregated parallel to their condensation (Russell & Howard, 2013). Another theory assumes FTA CAIs result from hit-and-stick collisions of CTA CAIs and minor melting (Rubin, 2012).

Some CAIs consist of several nodules covered in multimineral layers, the so-called Wark–Lovering rims (WLRs; e.g., Lorenz et al., 2019; MacPherson et al., 1982; Wark & Lovering, 1977). Different formation scenarios have been proposed, such as condensation (Bolser et al., 2016; MacPherson & Grossman, 1984; Wark & Lovering, 1977) or metasomatism on the parent body (MacPherson et al., 1982). Other studies proposed that flash-heating, which melted the outer region of the PPD, could be involved in WLR formation (Han et al., 2020; Wark & Boynton, 2001). It is also unclear whether WLRs formed immediately after CAI formation or about 1 Ma after the formation of the latter, as isotopic studies give conflicting information, which, however, could also be due to later isotopic disturbances in the nebula (Han et al., 2020).

Some igneous Type B CAIs have a disk- or bowl-shaped morphology (Ivanova et al., 2008), which was interpreted to result from aerodynamical deformation and shock flattening (Lorenz et al., 2019), or more complex scenarios which include ejection from the inner solar system and remelting during reentry at hypersonic speed (Liffman et al., 2016). Further relations between the morphology of CAIs and aerodynamical effects have been proposed in the most recent study of Zhang et al. (2021) in which the studied CAIs and AOs have an elongated or a bent fractal morphology, interpreted as resulting from movement induced by, for example, radial drift.

Experiments can help to understand early solar system processes, and different experimental approaches have been established. Microgravity experiments regarding particle aggregation in the solar nebula are well established and have already delivered valuable findings (e.g., Beitz et al., 2012; Blum, 2010; Blum et al., 2000, 2002; Steinpilz et al., 2020; Wurm & Blum, 1998). Experiments addressing the process of thermal annealing of early solar system materials, which are mostly focused on chondrule formation (Connolly & Libourel, 2005), have so far only been carried out on Earth and have mostly involved static samples.

To complement these different types of experiments, we developed a proof-of-concept experiment, which was carried out under long-term microgravity conditions aboard the International Space Station (ISS) to combine aggregation, heating, and thermal annealing of dust particles (Spahr et al., 2020). In this experiment, freely floating Mg_2SiO_4 dust particles were exposed to arc discharges inside a glass sample chamber with the aim to test how arc discharges influence the behavior of dust particles. A camera allowed the observation of the particles in real time and the sample material was analyzed after sample return to Earth. In the study presented here, we show the formation of aggregates using flash-heating under microgravity conditions, which can be linked to the formation of refractory inclusions with regard to their morphology and microstructure.

METHODS AND MATERIALS

ISS Experiments

The experimental setup is described in detail in Spahr et al. (2020). The experiment was set up inside a $10 \times 10 \times 15 \text{ cm}^3$ sized NanoRacks NanoLab, which was connected to the ISS by USB. The sample chamber consisted of quartz glass and two tungsten electrodes with a diameter of 1 mm were fused into the glass on opposite sides. The distance between the tips of the electrodes was approximately 2 mm. The sample chamber was loaded with 30 mg of the sample material and 100 ± 1 mbar Ar gas.

A detailed description of the generation and calibration of the arc discharges is given in Spahr et al. (2020). In total, 81 arc discharges with energies of 5–8 J and durations between 300 and 500 μs per discharge were induced, which exceed the energy necessary for a complete melting of the dust particles (Spahr, personal communication). The generation of the arc discharges also applied an electric field between the electrodes beginning approximately 2 min before the arc discharges. The area between the electrodes was filmed during the charging process and the arc discharges with

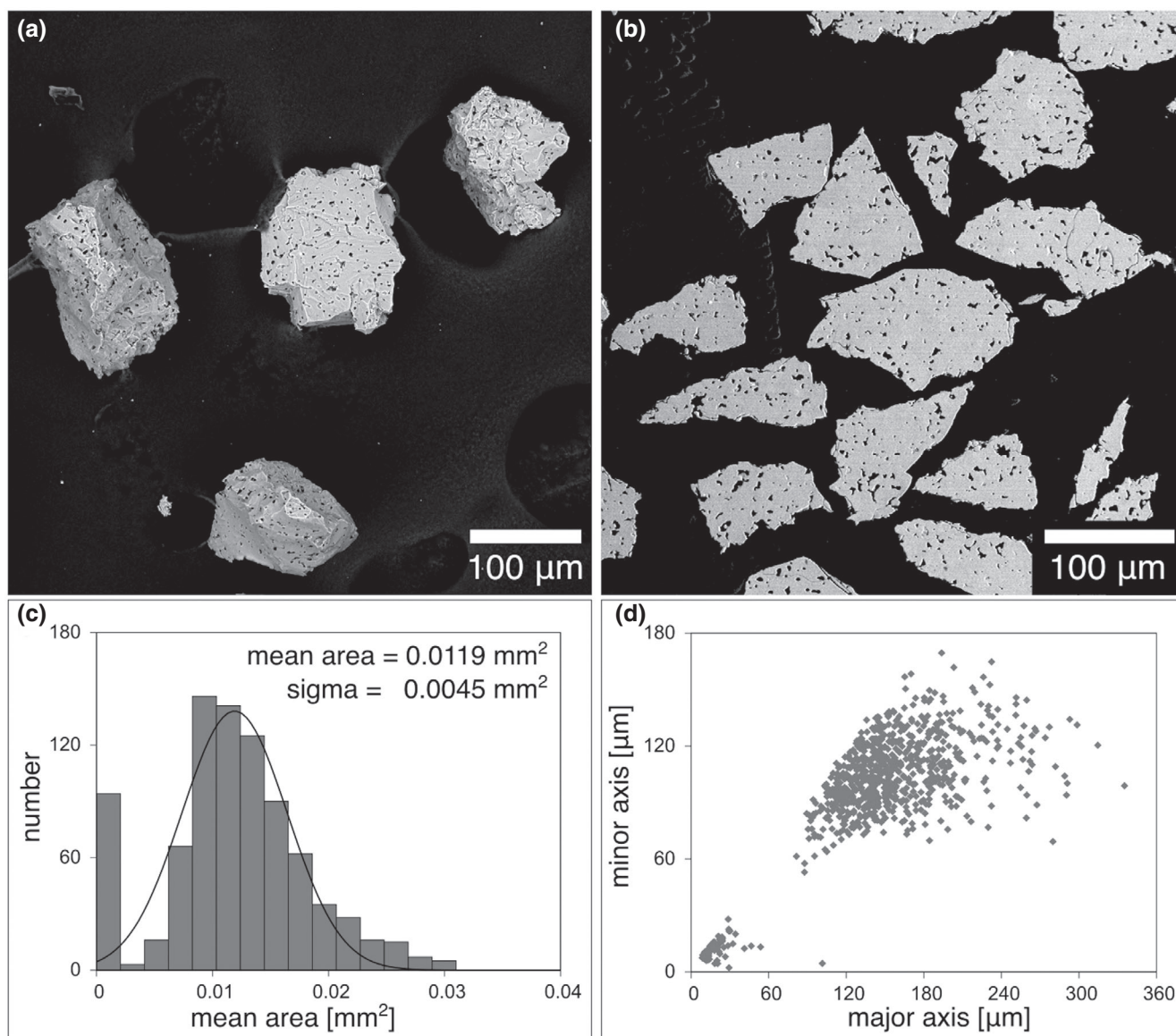


Fig. 1. Initial sample material. a) Focus-stacked representative porous initial dust particles used as starting material. b) Polished grains of the initial starting material. The particles have highly heterogeneous morphologies and a large amount of evenly distributed small pores. c) Histogram of the grain size distribution of a random sample containing 849 grains fitted with a normal distribution function. d) Correlation between the minor and major axes of best-fit ellipses of the initial material.

a Raspberry Pi V2 camera with a field of view (FOV) of 2.73×3.63 mm.

Sample Material

The initial sample material consisted of well-characterized synthetic forsterite particles (Spahr et al., 2020). Figure 1a shows a focus-stacked scanning electron microscopy (SEM) backscatter electron (BSE) image of three representative initial particles. Figure 1b shows several embedded and polished initial grains. Characteristics for the polished samples are numerous

evenly distributed small pores. The grains are irregularly shaped with rough surfaces. Electron backscatter diffraction (EBSD) analysis of the initial particles showed that the particles are fine-grained, consisting of crystals with (circular equivalent) diameters of 5–10 μm, with a few exceptions where larger crystals >20 μm are present (Koch, Spahr, Tkalec, et al., 2021). In the initial sample material, the crystals are randomly oriented within each grain.

The grain size analysis of the initial sample material was carried out using ImageJ (Rueden et al., 2017). Therefore, the grains were evenly distributed in a petri dish and photographed under an optical microscope.

The photographs were transformed into black and white images, where the particles are displayed as black areas with the shape of the particles. This type of image will be called a threshold image in the following text.

Figure 1c shows a histogram of the areas of a random sampling of 849 grains fitted with a normal distribution function. The mean area obtained from the fit is 0.012 mm^2 and, due to the heterogeneity of the particle shapes, the distribution is rather broad ($\sigma = 0.0045 \text{ mm}^2$). Figure 1d shows the correlation of the major to the minor ellipse axes, likewise indicating the variability of the particle morphologies. The grain size analysis of the transformed samples was undertaken with the same method.

The sample chamber was loaded with 30 mg of the sample material. Approximating the average volume of a single grain by a spherule with a diameter of $126 \mu\text{m}$ and a porosity of 10 vol%; the total number of particles is in the range of 10^4 particles, which represents a particle density of approximately $1.6 \times 10^{-3} \text{ g cm}^{-3}$.

Analytical Procedure and Sample Preparation

Scanning electron microscopy imaging was performed using a Phenom World ProX desktop SEM equipped with an electron backscatter detector at the Geoscience Institute at Goethe University. Energy-dispersive X-ray spectroscopy (EDX) was carried out with an integrated silicon drift detector (SDD) for a semi-quantitative characterization of the chemical composition. The noncoated samples were measured under low vacuum conditions; the polished and carbon-coated samples were measured under high vacuum conditions. For imaging, we used an acceleration voltage of 10 kV while for EDX analysis, a voltage of 15 kV was employed. Multiple BSE images were acquired with different focal planes and combined afterward with the Helicon Focus 7 Pro (Kozub et al., 2018) software from Helicon. EDX data were analyzed using the Phenom Pro Suite software.

EBSD fabric analysis is especially suited to identify structural and textural properties of materials and is increasingly employed as an analytic tool to investigate the remnants of solar nebular processes in planetary materials (Bland et al., 2011; Tkalcec et al., 2013). EBSD was performed at the Geoscience Institute at Goethe University Frankfurt with a JEOL scanning electron microscope JSM 6490. The SEM is equipped with a Nordlys II phosphor screen EBSD detector with Channel 5 software from Oxford Instruments and HKL Technology. EBSD was performed with an acceleration voltage of 15 kV, a working distance of 20 mm, and a Si-wafer as calibrant. EBSD data were acquired by automated mapping performed at step sizes of $0.8\text{--}1 \mu\text{m}$

with low gain, 2×2 pixel binning, and a mean angular deviation limit of $<1.3^\circ$. The pre-experiment, initial sample material, as well as the postexperiment resulting material were embedded in Araldite epoxy resin, polished with Syton polish and thinly coated with carbon. Following data acquisition, no noise reduction was performed on the acquired EBSD data. Contoured pole figures are displayed as multiples of uniform distribution (m.u.d.), with a half width of 10° .

Synchrotron-based micro-computer tomography (micro-CT) was performed at PETRA III (DESY) in Hamburg, Germany. All data were collected on the micro tomography beamline P05 (Moosmann et al., 2014; Ogurreck et al., 2013; Wilde et al., 2016), operated by Helmholtz-Zentrum Hereon, using a 15 keV beam monochromatized by a double crystal monochromator. The images were acquired with a $24\times$ magnification using a CMOS camera resulting in an approximately $1.8 \times 1.8 \text{ mm}^2$ FOV with a spatial resolution down to $1 \mu\text{m}$. Scans were performed with an acquisition time of 350 ms. A binning factor of 2×2 pixel resulted in a binned pixel size of approximately $0.61 \mu\text{m} \times 0.61 \mu\text{m}$. The samples were completely embedded in Araldite epoxy resin.

RESULTS

Analysis of the Video Recording

The experiments were filmed and the videos could be analyzed in order to observe the behavior of particles in response to arc discharges. Figure 2a shows the FOV prior to the arc discharge experiments. The tips of the electrodes are visible on opposite sides of the image. Some initial grains stick to the electrodes and sample chamber walls and appear out of focus in the center of the FOV. The space between the electrodes was empty. The first two arc discharges were induced while no particles were levitating between the electrodes. The arc discharges agitated the particles inside the sample chamber. Subsequently, the moving particles were attracted by the electric field between the electrodes and formed chains parallel to the electric field lines. The distance between the single chains of particles decreased with increasing charge buildup and the particles formed a dense aggregate levitating between the electrodes, which is shown in Fig. 2b. Some particles appear darker than others, which is due to the illumination conditions. The loose aggregate was destroyed by the arc discharges and the particles were agitated to a random particle motion. The particles were then attracted by the electric field between the electrodes, which was applied between two arc discharges and formed again chains of particles. However, the number of particle chains which formed

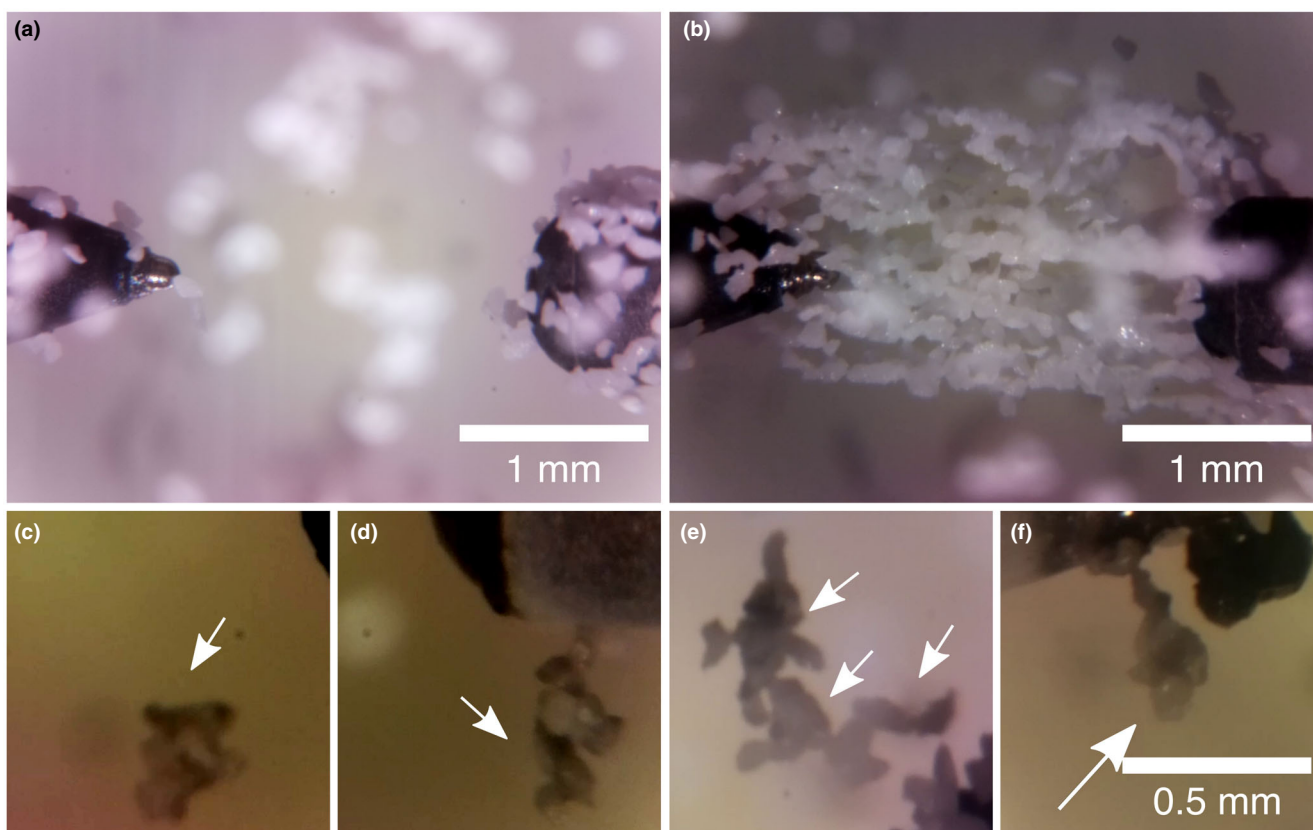


Fig. 2. Selected frames from the video material and particle aggregation during the experiment. a) The field of view prior to the arc discharge experiments. The tips of the electrodes are shown on opposite sides of the image. Some initial particles stick to the electrodes and the sample chamber walls. b) The particles formed chains along the field lines between the two electrodes prior to the third arc discharge. c) A massy aggregate (white arrows) appeared after the 16th arc discharge (contrast enhanced). d) An elongated aggregate (white arrows) appeared after the 34th arc discharge (contrast enhanced). e) Three fused aggregates after the 75th arc discharge (white arrows). f) An elongated, bulbous aggregate (white arrow) detected after the 81st arc discharge (contrast enhanced). Scale bar for (c)–(g) is displayed in (f). The aggregates appear darker because of different automatic settings of the camera and tungsten contaminations on the particles and sample chamber walls, which sputtered from the electrodes during the arc discharges. (Color figure can be viewed at wileyonlinelibrary.com.)

between the electrodes decreased with the number of arc discharges to approximately two to three chains of particles. In total, particle chains were present prior to 27 arc discharges.

The first small fused aggregate (two to three fused particles) was observed after the fourth arc discharge and the number of observed aggregates increased with increasing arc discharges. The aggregates were observed either when they crossed the FOV agitated by the discharges or when they were attracted by the electrodes when the capacitors were charged. Selected frames from the video material showing some representative aggregates are shown in Figs. 2c–g. These aggregates appear darker than the initial grains due to different automatic lighting adjustments of the camera and because of tungsten contamination on the particles and sample chamber walls, which sputtered from the electrodes during the arc discharges.

The massy, approximately 300 μm sized aggregate in Fig. 2c crossed the FOV after the 16th arc discharge. Figure 2d shows an elongated aggregate attracted to the electrode after the 34th arc discharge. Figure 2e is a frame shot from the video after the 75th arc discharge, where three different aggregates levitated parallel to the electric field lines between the electrodes similar to the particles in Fig. 2b. One of these aggregates is elongated (top), while the other two aggregates are curved. The elongated, bulbous aggregate in Fig. 2f appeared after the last arc discharge.

It was not possible to assign a specific aggregate to a specific discharge event or to distinguish whether the particles melted inside the plasma channel or by thermal radiation due to the frame rate. The focus plane of the camera objective was very small and many aggregates crossing the FOV were not in focus to allow subsequent

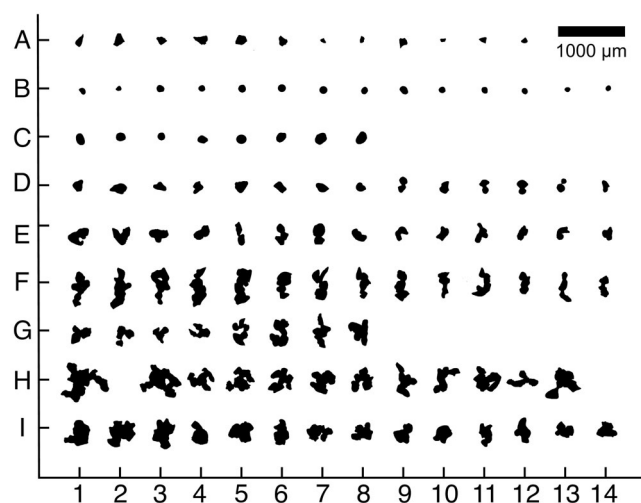


Fig. 3. Threshold image of the initial grains and formed objects. Different types of experimental outcomes were detected. A: Representative initial sample grains. B and C: Melt spherules. D and E: Small aggregates. F: Elongated aggregates. G: Small fluffy or three-winged aggregates. H: Fluffy aggregates with a three-winged boomerang-shaped morphology. I: Aggregates that are completely massy or have a massy center. The object numbers in this diagram serve for identification of the specific objects referred to in the following analysis.

identification (and discharge allocation) at the end of the experiment.

Morphology Analysis of Fused Aggregates

After sample return, the transformed objects were picked from the total sample material inside a petri dish. The aggregates were photographed and selected images were transformed into threshold images using ImageJ. More than 100 newly formed objects including single spherules and fused aggregates could be detected. Due to the large amount of sample material in the recovered sample chamber, it seems likely that this number is underestimated for melt spherules and small aggregates that could be hidden in the remaining dust.

The formed objects can be divided into different groups according to their morphological characteristics. Figure 3 shows the threshold images of the initial grains (A) and the experimentally transformed objects (B–I). The coordinate numbers in this diagram are used as reference frame for identification of the specific aggregates described in the following text. It is important to mention that these threshold images are only two-dimensional representations of three-dimensional objects, therefore the subdivision of the objects into different morphological groups is rather a rough estimation than an exact classification scheme.

Table 1. Ratio of the longest (*b*) versus shortest (*c*) dimensions of the elongated aggregates (Fig. 3 row F).

No.	F1	F2	F3	F4	F5	F6	F7
<i>b/c</i>	1.9	1.9	1.9	2.2	2.1	1.9	2.1
No.	F8	F9	F10	F11	F12	F13	F14
<i>b/c</i>	2.3	2.0	2.2	1.7	1.8	2.3	2.3

However, some important and systemic characteristics of the formed objects could be observed.

The most abundant sample type group consists of 21 single melt spherules (rows B and C) in addition to five melt spherules that are fused to other single particles (rows C and D). This number is probably underestimated, because not all melt spherules could be detected among the high amount of initial particles. Another large group represents small aggregates consisting of two to four grains, which are shown in rows D and E. The aggregates displayed in row F represent aggregates with an elongated morphology. Table 1 summarizes the ratios between the longest (*b*) and shortest (*c*) dimension of the 14 elongated aggregates shown in row F. The mean *b/c* ratio is 2.1 ± 2 .

The most conspicuous morphology is displayed by the aggregates in rows G and H. Their morphology is characterized from curved fused chains of particles (e.g., #G5, G6); very irregular fractal structures (e.g., #H5, H6); up to clear, three-winged, “boomerang-shaped” morphologies (#H1, #H4). However, due to the limitation of this classification scheme, some aggregates shown in row G could be also grouped to row H and vice versa. Furthermore, some aggregates shown in row F could also be assigned to G or H.

Row I includes aggregates, which consist of several fused grains merged to one massy object, where the different initial grains could no longer be distinguished. Some single grains were fused to the surface. To simplify, these aggregates will be called massy aggregates in the following text.

The area sizes of the different aggregates are plotted in the histogram in Fig. 4a, the correlation of the major to the minor ellipse axes of the newly formed objects in comparison to the initial sample material in Fig. 4b. There is a strong decrease in frequency toward larger sizes, especially considering the number of single melt spherules is probably underestimated. The total area of all aggregates divided by a mean aggregate diameter of 126 μm results in approximately 300–400 reacted initial grains, which is 3–4% of the initially loaded sample amount.

Micro-CT Analysis

Some aggregates were analyzed with synchrotron micro-CT to study their morphology and internal

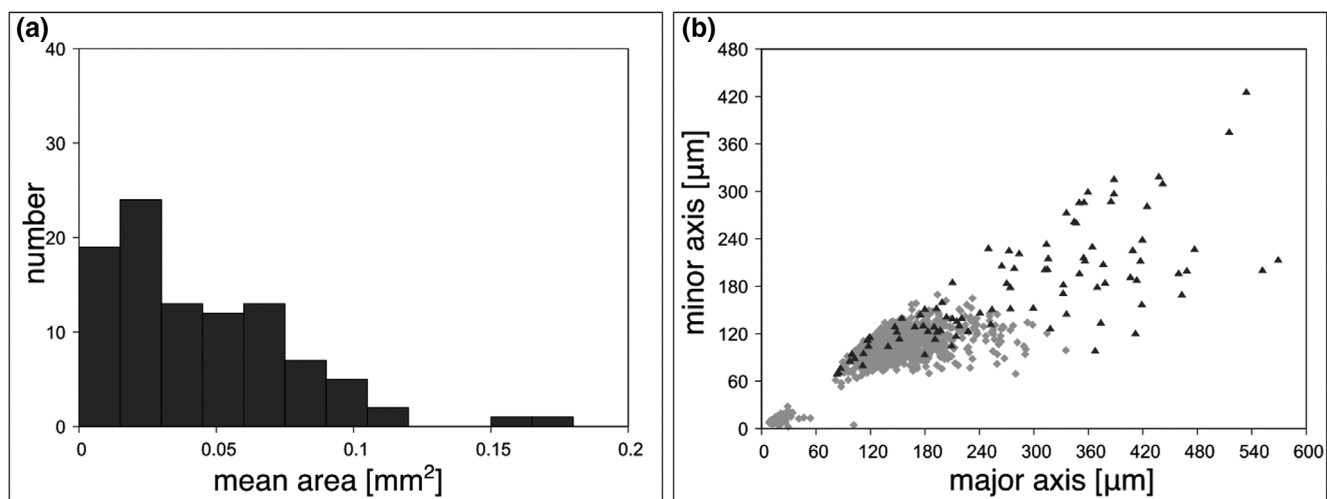


Fig. 4. Size analysis of the newly formed objects. a) Histogram of the area size distribution. b) Major axis versus the minor axis of the approximated ellipsoids of the resulting material (dark gray) in comparison to the sizes of the initial material (light gray).

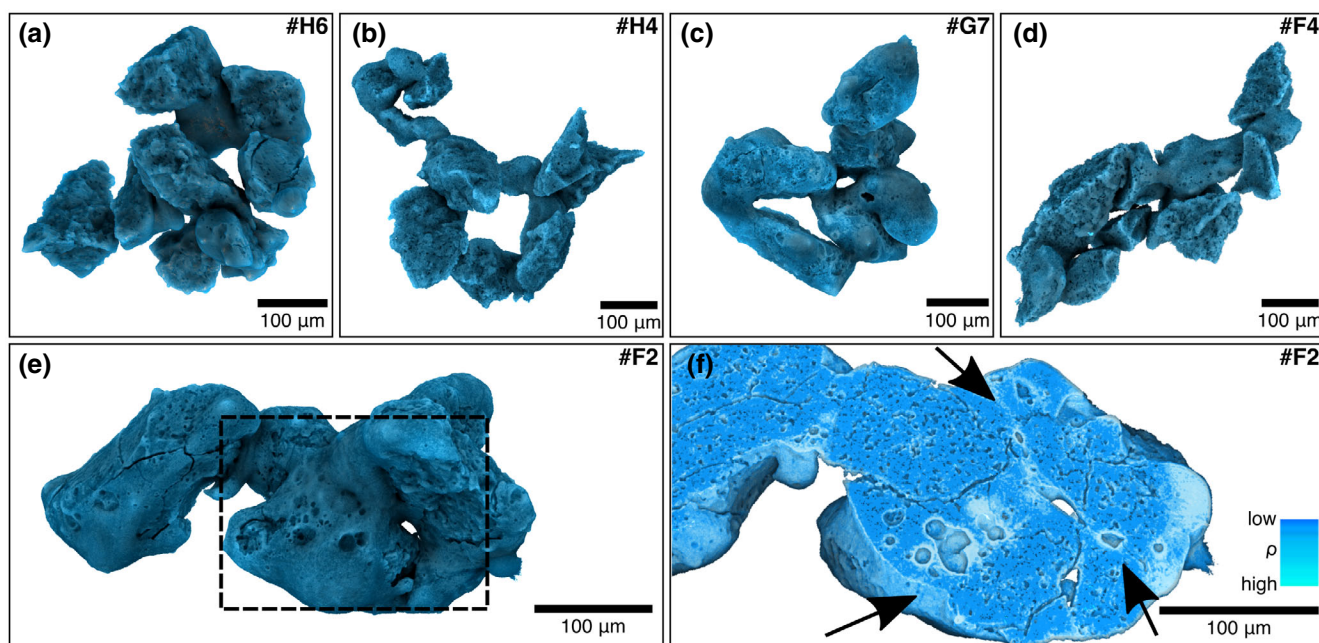


Fig. 5. CT projection of some generated fused aggregates. a–c) Aggregates with a boomerang-shaped morphology. d, e) Elongated aggregates. The aggregate in (d) consists mostly of grains with the initial angular and porous surface. The surface of the aggregate in (e) is mostly smooth with a few porous areas. f) A virtual slice through the aggregate in (e) (black dash square) reveals a generally more porous interior. The triple junction in the middle of the right part of the aggregate suggests that at least three grains were fused and form a triple junction. While the centers of the fused grains appear unprocessed, the interstitial areas (marked by arrows) have lost their original pore structure and instead, larger, spheroidal voids are present. Furthermore, these areas appear brighter, which is indicative of a higher density and is probably due to tungsten precipitation. The outlines of the pores and cracks appear bright because of edge enhancement due to coherence. (Color figure can be viewed at wileyonlinelibrary.com.)

structure. Figures 5a–c show aggregates from rows G and H with fractal morphologies, whereas Figs. 5d and 5e show elongated aggregates (from row F). The aggregates shown in Fig. 5 consist of approximately 7–10 initial

particles. The aggregate in Fig. 5d consists mostly of angular grains with porous surfaces similar to the initial starting material. The surface of the aggregate in Fig. 5e is mostly smooth. Figure 5f shows a virtual slice through

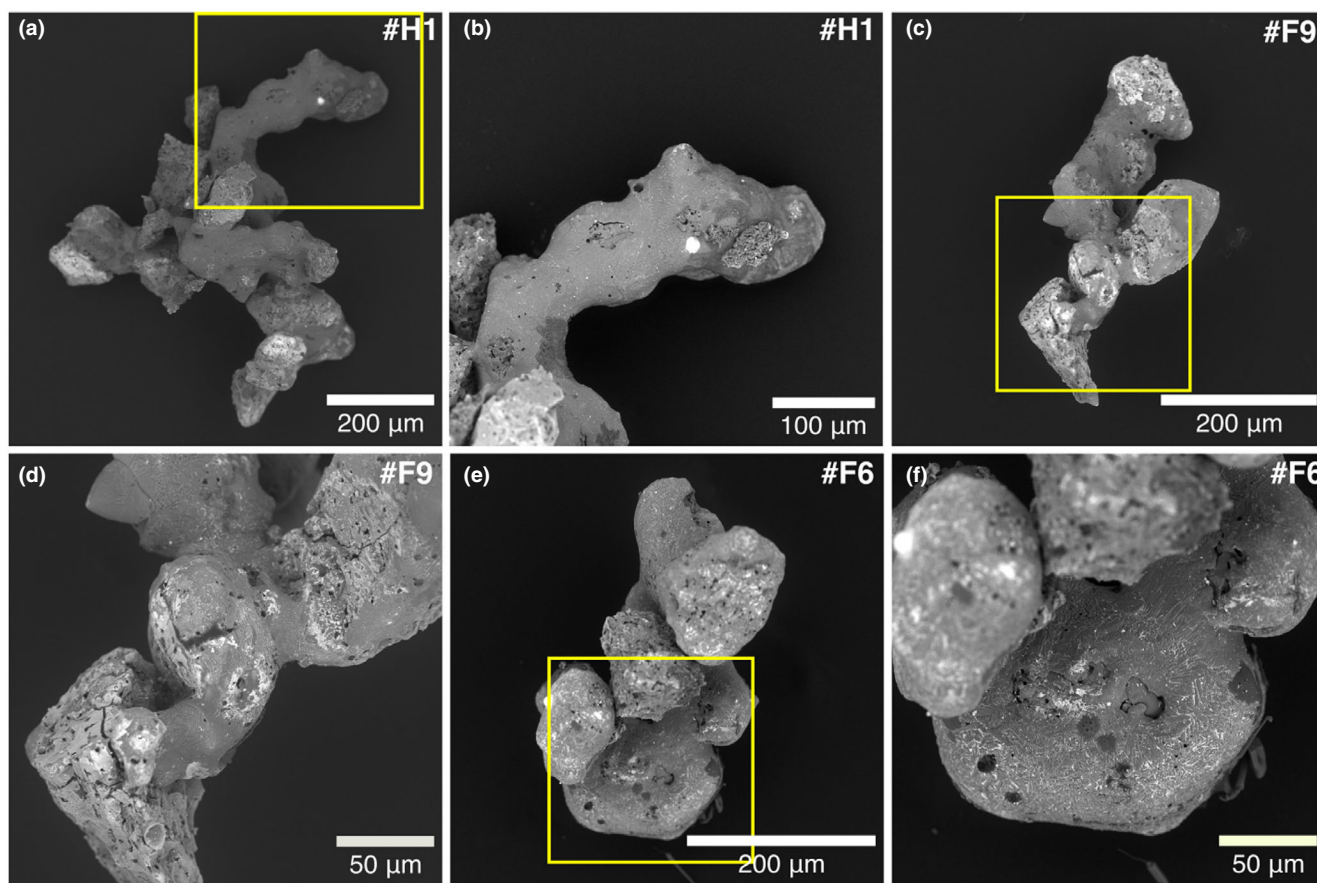


Fig. 6. Focus-stacked SEM BSE images of representative fused aggregates. a) Aggregate with a nearly perfectly three-winged, boomerang-shaped morphology. b) Close-up of the largest wing showing a molten surface with tungsten precipitation lines. Opening in the surface reveals a more porous interior. c) Elongated aggregate. d) Close-up of the aggregate in (c) showing completely molten inner region between particles. e) Elongated aggregate with a flat, molten disk. f) Close-up of the disk with tungsten precipitation. Yellow boxes in (a), (c), and (e) denote the positions of the close-up images in (b), (d), and (f), respectively. (Color figure can be viewed at wileyonlinelibrary.com.)

the aggregate in Fig. 5e (black dash square), revealing that at least three initial grains were fused. The grain boundaries (white arrows) are molten, displaying larger, spherical pores and a slightly higher density (brighter in the image) than in the unmolten areas. The three boundaries meet in the center in a triple junction (Fig. 5f, center).

SEM Analysis

SEM analysis was also used to study the morphology and composition of the aggregates. The analysis of the single melt spherules was part of an earlier study (Koch, Spahr, Tkalec, et al., 2021). Figure 6 shows focus-stacked BSE images of some representative elongated fractal-shaped aggregates. All aggregates consist of dust grains with various degrees of melting. Figure 6a shows the largest formed object, which has formed from approximately 20 initial grains.

The object has an almost perfectly symmetric, three-winged morphology with a diameter of approximately 720 μm . Figure 6b shows a close-up of the longest arm, which consists of a bent chain of fused grains. A high percentage of the surface is molten material; however, the internal structure is visible through some cavities in the surface.

Figure 6c shows one of the elongated aggregates with a length of 425 μm . The surface of the grains in the middle area of the aggregate was completely molten (Fig. 6d), the outer grains show the initial surface structure. The object in Fig. 6e has a length of approximately 500 μm . One part of the aggregate consists of a 170 μm sized flat disk (Fig. 6f) displaying a very strong tungsten pattern on its surface.

In general, the molten surfaces of the different aggregates show fine lines of tungsten precipitation similar to Fig. 6f, which appear bright in the BSE images. This precipitation arises from evaporation of

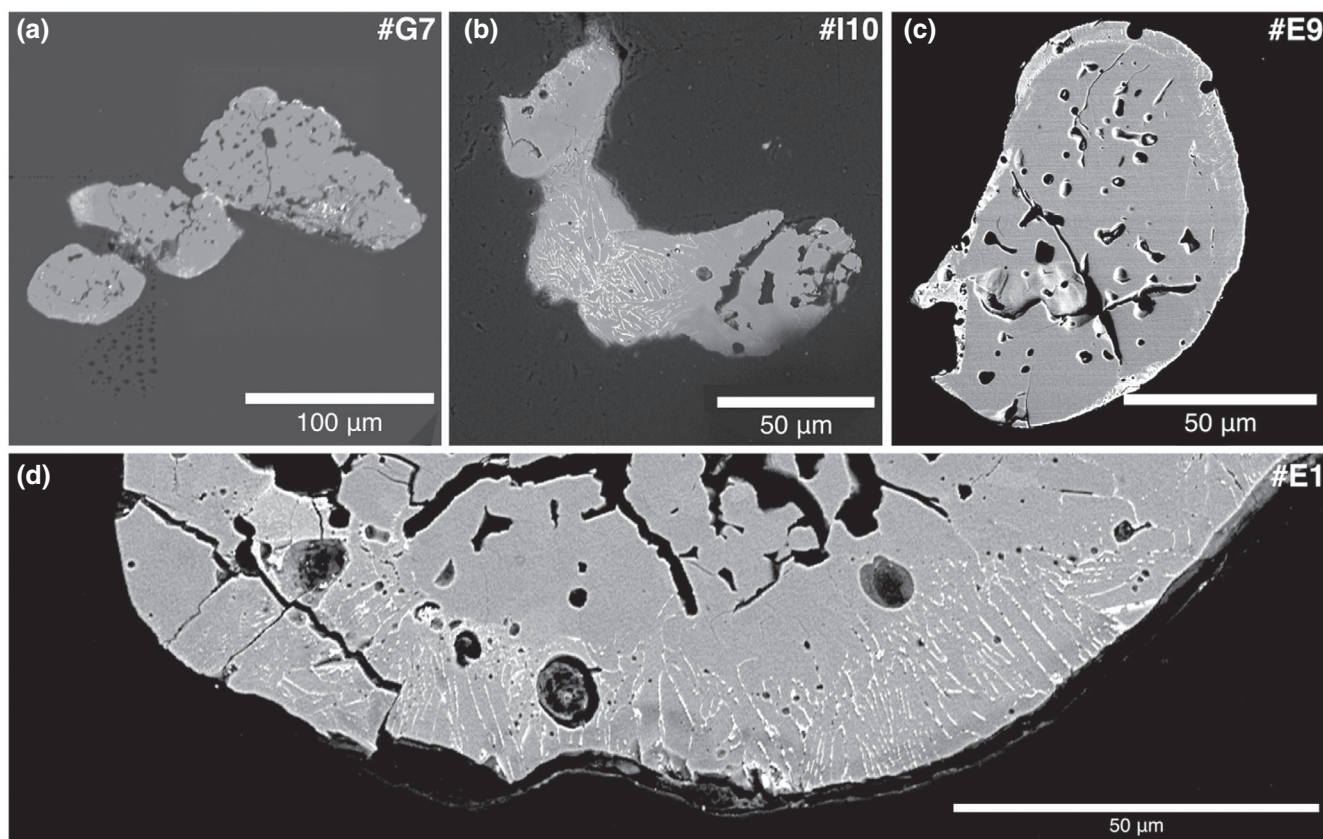


Fig. 7. SEM analysis of polished aggregates. The melted areas and grains of the aggregates can be identified by the absence of the initial pore structure, by some sort of fusion crust on the surface, and by tungsten inclusions. The molten areas of the particles show tungsten inclusions in round inclusions and precipitations along the grain boundaries. The tungsten, which was evaporated from the electrodes during the arc discharges, interacted with the melt and precipitated along the grain boundaries during crystallization. a) Three grains which still reveal the original pore structure and were only fused on the surface. b) Three fused aggregates with three different thermal histories. The center grain displays abundant tungsten precipitation lines and was probably completely molten. The upper grain has lost its initial pore structure but includes less tungsten. The third grain shows molten outer regions, but the initial pore structure the interior regions. c) Particle of aggregate #E9, which is completely surrounded by a tungsten-bearing igneous rim. The inner part of the grain is nearly unprocessed; however, the pores have slightly changed and appear more round than in the initial material. d) Close-up of one of the fused grains of the fused aggregate #E1. The grain shows an igneous rim with a thickness of approximately 17–22 μm displaying the typical tungsten precipitation lines and spherical pores indicative of melting.

the tungsten electrodes. However, as the aggregates were not carbon-coated prior to SEM analysis, surface charging may also be responsible for some bright artifacts.

Some aggregates were polished before SEM analysis (Fig. 7). The polishing reveals different thermal histories of particles in more detail and even grains that are directly fused to each other have experienced very different degrees of melting. The melted areas and grains can be identified by the absence of the initial pore structure, by spherical pores, by some sort of fusion crust on the surface, and by tungsten inclusions. The molten areas of the particles show tungsten inclusions in round inclusions and precipitation along the grain boundaries. The tungsten, which was

evaporated from the electrodes during the arc discharges, interacted with the melt and precipitated along the grain boundaries during crystallization.

Figure 7a shows a grain which is only molten on the surface next to two nearly unprocessed initial particles. Figure 7b shows three or four fused grains. One grain was probably completely molten with very few tungsten inclusions on one side and some round pores. The elongated grain in the middle is interspersed by tungsten precipitation next to a nearly unprocessed particle. Figure 7c shows a grain from aggregate #E9, which underwent melting on the surface, while the inner structure of the grains underwent only light thermal annealing. Figure 7d shows a close-up of one of the fused grains of the fused aggregate #E1. The grain

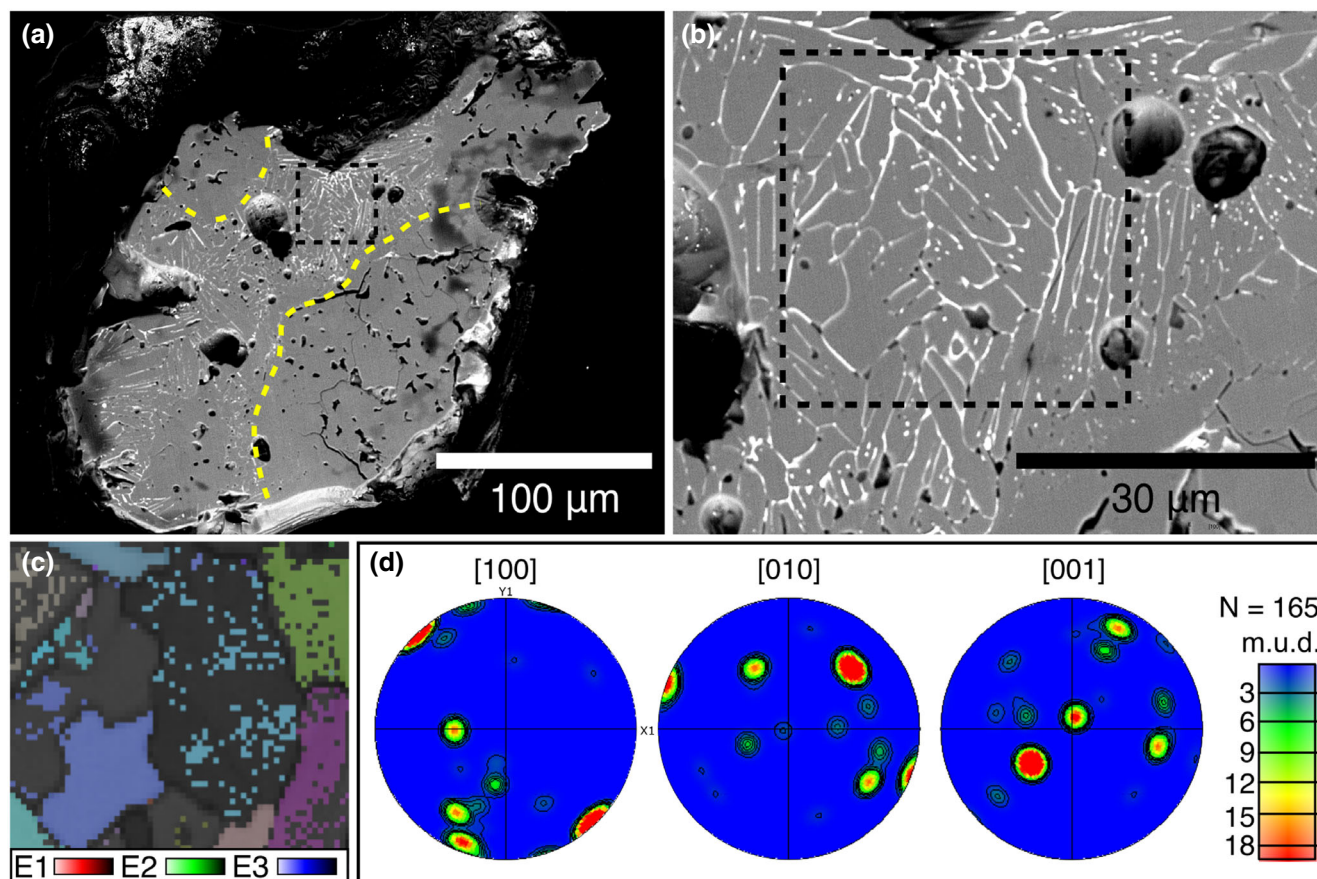


Fig. 8. SEM and EBSD analyses of a polished massy aggregate #112. a) SEM BSE overview of the polished aggregate. The yellow dashed lines indicate the boundaries between molten and original sample material. b) A close-up of the molten area (black dashed square). The bright lines and inclusions represent tungsten precipitation. c) EBSD band contrast image with overlying all-Euler angle map of forsterite of the area marked by the dashed square in (a) and (b). E1, E2, and E3 represent the Euler angles. d) Stereographic projections of EBSD data of the area shown in (c). (Color figure can be viewed at wileyonlinelibrary.com.)

shows an igneous rim with a thickness of approximately 17–22 μm displaying the typical tungsten precipitation lines and spherical pores indicative of melting.

Figure 8 shows the SEM and EBSD analysis of the polished aggregate #112. The aggregate has a massy core and is droplet-shaped. Its size suggests that it fused from four to six initial grains. Figure 8a shows an overview of the polished aggregate. Several areas with the original pore structures could be identified (yellow dashed lines). Figure 8b shows a close-up of the molten area between the initial areas. The molten area shows the typical tungsten precipitation pattern with parallel lamellae. This area was studied with EBSD in more detail and all indexed patterns were indexed as forsterite. Figure 8c shows the band contrast image superimposed with an all-Euler angle map. The grain sizes identified in the band contrast image, displayed by black boundaries from the overlapping of two adjacent signals and defined by a misorientation threshold of 10° ,

are larger than those originally inferred from the tungsten precipitation patterns. This indicates that misorientation angles between the intragrain tungsten lamella are less than 10° . The all-Euler map confirms the presence of some large grains, several of which display well-indexed interiors with negligible intragrain misorientation, whereas others, for example the large center grain, reveal several nonindexed areas. In the latter case, however, all indexed points show the same uniform all-Euler orientation confirming the single-grain identification shown by the grain boundaries of the subimposed band contrast map. The crystallographic orientations of these large forsterite grains are revealed by pole figures (Fig. 8d) contoured by m.u.d. set at maximum 12. Because the original data was not subjected to any noise reduction, the few tight point maxima (red) likely reflect duplication (nonadjacent points measured from the same large grain but identified as individual grains) in grains where indexing

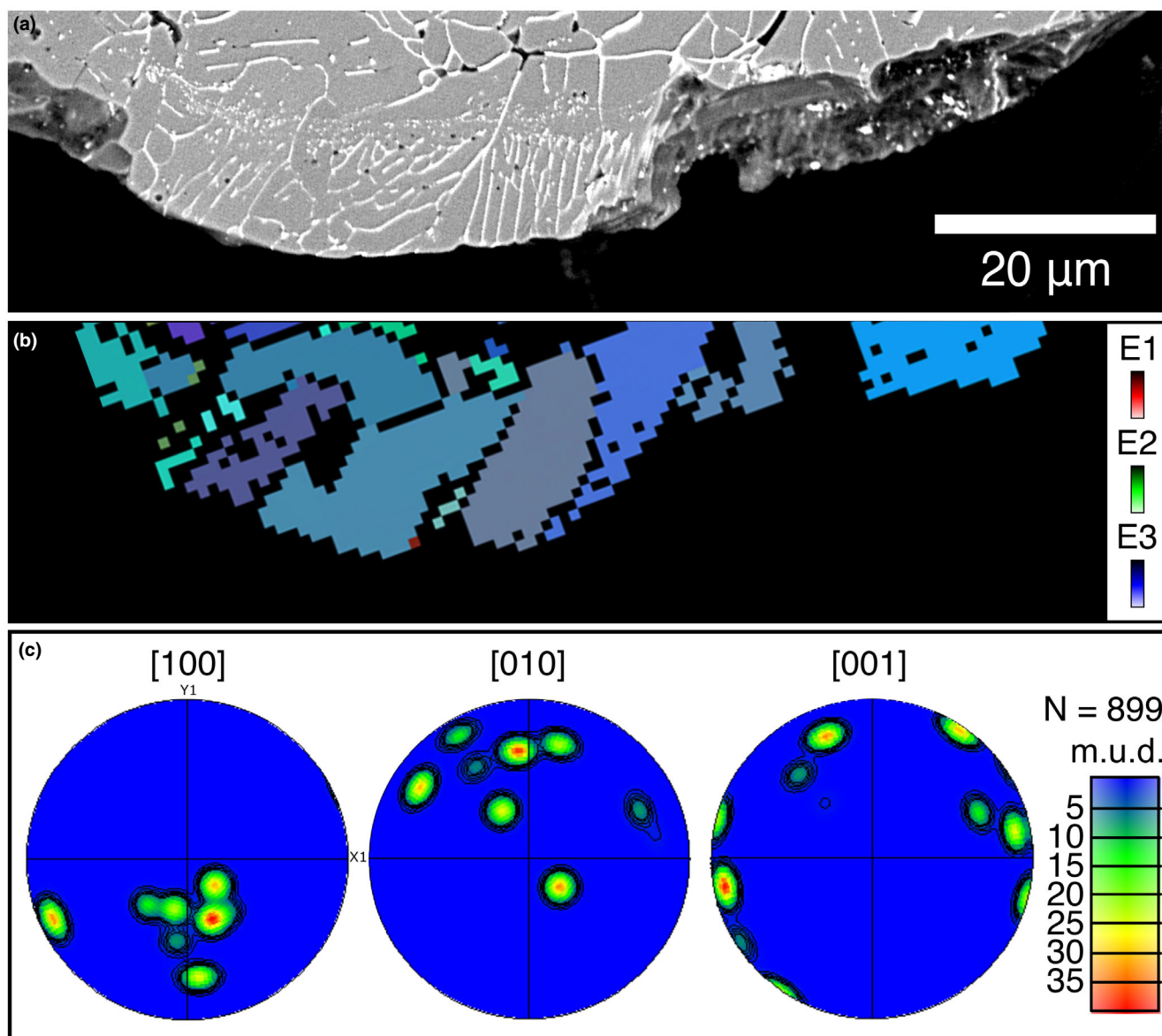


Fig. 9. EBSD analysis of the igneous rim of an aggregate. a) BSE image of the rim of one particle of aggregate #E1. The lines that appear white in the BSE image represent tungsten precipitation. Grains show a tungsten-lamellae (TL) and tungsten-free (TF) zone. b) EBSD all-Euler map displaying the grain boundaries reveals that the observed sets of mostly parallel tungsten lamellae are intracrystal. c) Stereographic projections of EBSD data of the rim. The grains show preferred orientation in all three crystallographic axes. (Color figure can be viewed at wileyonlinelibrary.com.)

was not continuous. Thus, each large red m.u.d. maximum contour is interpreted as a single grain. The crystallographic [100] axes plot as broad N-S point maxima of several grains and the [010] axes possibly as a broad E-W girdle, although the latter should be seen with caution due to the small number of grains involved.

One of the igneous rims (particle #E1) was also studied with EBSD. The BSE image in Fig. 9a reveals that the rim of particle #E1 is clearly different

compared to the initial material. Tungsten precipitation is strongly present in grain boundaries (Fig. 9a) and often forms parallel lamellae perpendicular to the particle surface. In addition, a multitude of tiny tungsten spots appear to be arranged in a linear layer parallel to (and about 14 μm inside) the particle rim. This tungsten layer runs perpendicular to the tungsten lamellae, which it appears to truncate, thus dividing each grain into the tungsten-lamellae-bearing (TL) and tungsten-free (TF) zones.

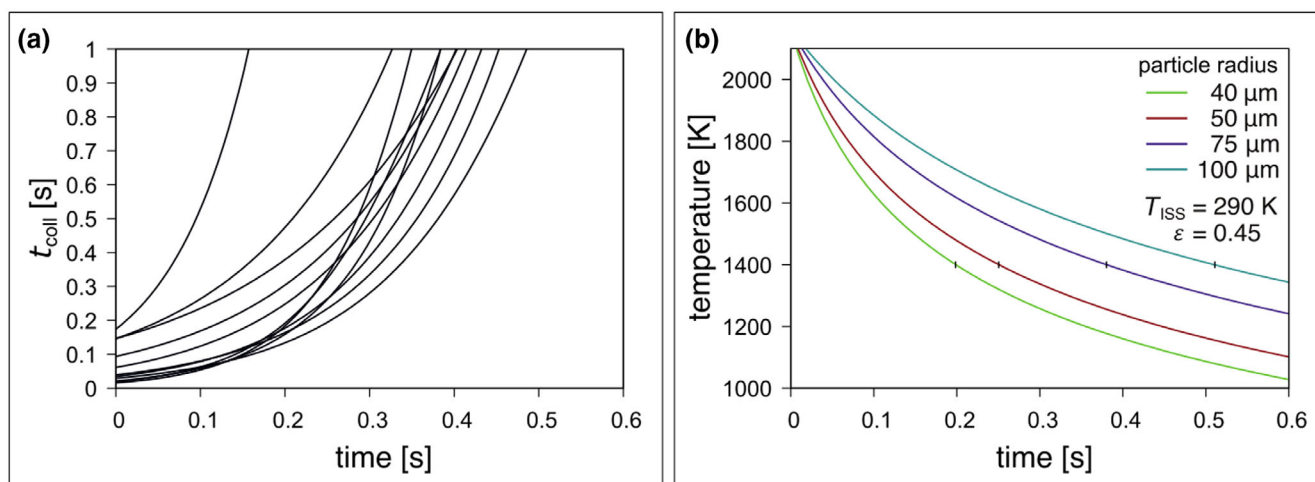


Fig. 10. Collision times t_{coll} of particles inside the sample chamber and cooling rates of the particles after arc discharges. a) t_{coll} versus the time after arc discharges is plotted for several grains after different arc discharges. b) Calculated temperatures of particles with different radii versus time after arc discharges inside the sample chamber. (Color figure can be viewed at wileyonlinelibrary.com.)

The corresponding EBSD all-Euler phase map reveals a number of large grains all aligned with their longest dimension perpendicular to the surface. The crystal directions of the grains plotted in the pole figures in Fig. 9c confirm a strong crystallographic preferred orientation of all grains. The tungsten lamellae are oriented perpendicular to the particle surface and parallel to the longest dimension of the grain in each case, dividing the part of the grain closest to the rim into parallel zones with negligible misorientation to one another.

Time Scales of Aggregation

The duration of aggregate formation in the experiments depended on the collision time scale and the cooling rates of the particles. The collision time t_{coll} describes the mean time of a grain between two collisions (Marrocchi et al., 2019; Nakagawa et al., 1981) and can be expressed as Equation 1:

$$t_{\text{coll}} = \frac{1}{n_p 4\pi a^2 \Delta v_{\text{coll}}} \quad (1)$$

where Δv_{coll} is the particle–particle velocity, which is assumed to be similar to the collision velocity; a is the mean particle radius; and n_p is the particle density ($5500 \text{ particles cm}^{-3}$). The particle velocities v_{coll} after arc discharges were determined for different particles from the videos (see Koch, Spahr, Merges, et al., 2021). The measured particle velocities are in the range of $>25 \text{ mm s}^{-1}$ with a subsequent exponential deceleration due to gas drag. We calculated t_{coll} for

different velocity profiles using the fitting parameters from Koch, Spahr, Merges, et al. (2021). Figure 10a shows some representative collision times of particles after arc discharges dependent on the time after the discharge events. Immediately after the arc discharge, the mean time between two collisions of a particle is in the range of 0.01 and 0.2 s. Consequently, aggregates which consist of approximately 20 particles could have formed in 0.2–4.0 s. However, the particle size a will increase with aggregate formation, which also decreases the number of particles in the sample chamber. However, these effects are neglected in the calculations.

Another limitation for the duration of aggregate formation is the cooling rate of particles, because the particles have to be plastic to fuse in collisions. The lower temperature limit for the formation of compound chondrules was defined to be 1400 K, which represents the lowest temperature where silicate melts were present in chondrule melt (Bischoff et al., 2017; Ciesla et al., 2004). We used this temperature as a lower limit for the calculation of the time scale of aggregate formation in the experiment, because the initial sample material consists of Mg_2SiO_4 .

The cooling rates of chondrules melted by lightning are usually modeled by radiative cooling of a gray body (Equation 2) (Morris & Desch, 2010). The temperature of the chondrule analogue after the arc discharge is given by the liquidus temperature of forsterite of 2163 K (Bowen & Schairer, 1925) and the temperature aboard the ISS is estimated to be 290 K. Equation 2 gives the change of the internal energy U of a radiating spherical gray body with time:

$$\frac{\partial U}{\partial t} = \epsilon \cdot \sigma \cdot A \cdot (T_{\text{sample}0}^4 - T_{\text{ISS}}^4) \quad (2)$$

where U is the internal energy, t is the time after the heating pulse in s, ϵ is the emissivity (for reference, a black body has an emissivity of 1), σ is the Stefan–Boltzmann constant, A is the surface area of the spherule, and $T_{\text{sample}0}$ is the temperature of the heated spherule at time 0 and T_{ISS} is the temperature of the surrounding, both in K. ΔU for a short dt can be obtained using Equation 3.

$$\Delta U = \epsilon \cdot \sigma \cdot A \cdot (T_{\text{sample}}^4 - T_{\text{ISS}}^4) \cdot dt \quad (3)$$

The change in U can also be described by means of the temperature-dependent specific heat capacity $c_p(T)$ in $\text{J mol}^{-1} \text{K}^{-1}$, the change in temperature of the spherule ΔT in K, and the amount of substance in mol (Equation 4). The amount of substance n is calculated for different spherule sizes using the volume of the spherule, the density of forsterite (3.275 g cm^{-3}), and the molar mass of forsterite ($140.693 \text{ g mol}^{-1}$) (Anthony et al., 2018).

$$U = c_p(T) \cdot n \cdot (\Delta T) \quad (4)$$

Combining Equations 3 and 4 gives an expression for the change in temperature of the spherule during a short time of radiation (Equation 4).

$$\Delta T = \frac{\epsilon \cdot \sigma \cdot A (T_{\text{sample}0}^4 - T_{\text{ISS}}^4) \cdot dt}{c_p(T) \cdot n} \quad (5)$$

The resulting ΔT is subtracted from $T_{\text{sample}0}$ to derive the new temperature of the spherule $T_{\text{sample}1}$. Using this new temperature, the calculations are iterated N times until $T_{\text{sample}N}$ is sufficiently close to T_{ISS} (291 K in this case). The specific heat capacity $c_p(T)$ in Equation 4 is calculated for each iteration step with the data from the NIST Standard Reference Database (see NIST, 2020).

The cooling rates of the particles were determined to be 10^7 – 10^4 K h^{-1} shortly after the arc discharges (Koch, Spahr, Tkalec, et al., 2021). Figure 10b shows the temperature of the particles with different sizes after the discharge events. The particles were cooled to 1400 K in between 0.2 and 0.5 s. It is important to mention that the model was calculated for solid droplets. However, forsterite melt drops should have high temperatures ($<2163 \text{ K}$) and similar high cooling rates at these temperature. Therefore, this model also provides an appropriate estimation for the aggregation times. Thus, it is likely that aggregate formation in the experiment was a very fast process of $<0.5 \text{ s}$ after the

discharge events, which is in accordance with the results from the collision time determination.

However, these calculations only work for fully molten, spherical particles and partially molten grains could cool much faster. Therefore, partially molten grains had to collide with other particles much faster than fully molten particles and therefore it is likely that aggregates formed from particles which were very close to each other during the discharge event, perhaps the particles which were aggregated in the electric field prior to the arc discharges. However, it was not possible to observe the collisions of particles due to the frame rate.

Morphology Analysis of Natural CAIs

To compare the morphology of the aggregates formed in the experiment with natural CAIs, a random sample of representative CAIs in the CV3 chondrite NWA 13656 were analyzed regarding their morphology. Figure 11 shows optical microscopic images of different types of fractal inclusions. Figure 11a shows an inclusion with three to four wings. Figures 11b and 11c show inclusions which have a massy center and several attached nodules. Figure 11d shows a very elongated inclusion.

Threshold images of the different inclusions in NWA 13656 were used for the morphology analysis. Figure 12 shows the threshold images of the NWA 13656 inclusions sorted according to their morphology: small inclusions consisting of only a few single nodules (J), elongated inclusions (K), bent fractal inclusions (L), fractal aggregates with four- and three-winged morphology (M), and inclusions with a massy center (N). However, it should be noted that they represent two-dimensional cross sections of CAIs and the three-dimensional morphology could show another morphology-type.

Figure 13 shows the size analysis of the natural inclusions. It is important to mention that we used a random sample of CAIs, which resemble the three different aggregate types produced in the experiment. NWA 13656 includes also a wide range of spherical or completely molten CAIs in each size. The histogram in Fig. 13a shows a heterogeneous distribution of the natural CAI sizes. However, this size distribution is biased due to the sample preparation, which only displays a two-dimensional image of the CAIs. Figure 12b shows the plotted minor versus major ellipsoid axis of the best-fit ellipsoids of the natural CAIs in comparison with the initial starting material of our experiment and the experimentally formed aggregates. The natural CAIs plot in the same range relative to the experimentally formed aggregates standardized by a factor of 5.

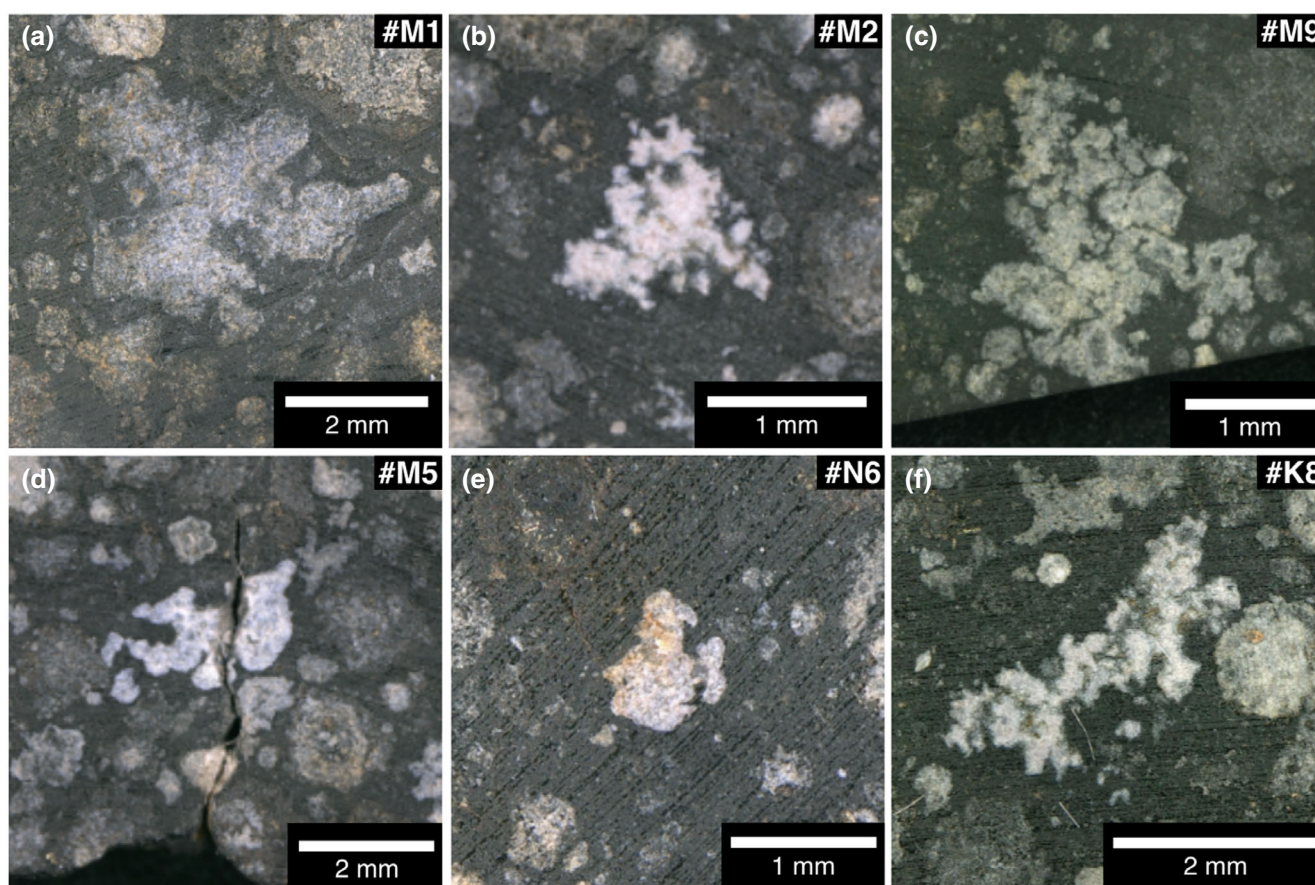


Fig. 11. Photographs of irregular inclusions on slices of NWA 13656. a) Inclusion with four wings. b) Tringle-shaped inclusion. c) Three-winged inclusion. d) Inclusion with a massy center and two attached nodular wings. e) Inclusion with a massy center and several attached nodules. f) Elongated inclusion. (Color figure can be viewed at wileyonlinelibrary.com.)

Table 2 shows the ratios between the longest (*b*) versus the shortest (*c*) direction of the natural CAIs. The values are generally in the same size range as those of the experimentally formed aggregates (Table 1) with some outliers of higher ratios >3 , which could be a cutting effect. The mean value of the ratios excluding the outliers is 2.1 ± 0.3 .

DISCUSSION

In the experiment aboard the ISS, two types of experimental outcomes were produced, single melt droplets and fused aggregates. While the melt spherules have been discussed in their role as chondrule analogs in a previous study (Koch, Spahr, Tkalcec, et al., 2021), we concentrate here on the fused aggregates.

Aggregate Formation in the Experiment

The early appearance of aggregates also argues for a formation of these aggregates beginning during the

first arc discharges. Most aggregates produced in the experiments show some typical morphologies, which can be broadly divided into elongated aggregates, fluffy aggregates with curved and boomerang-shaped morphologies, and massy aggregates. These aggregates were formed from collisions between particles which had experienced different degrees of melting from pristine unmolten and/or melted particles. Still ductile, these aggregates moved with high velocities in various directions and some aggregates transformed into the typical fractal or boomerang-shaped morphologies. The calculated cooling rates and collision times indicate an aggregate formation in $\ll 0.5$ s, which also implies that the aggregates solidified while still in motion.

Another question which arises is whether a single aggregate was formed after a single flash-heating event or by collisions of small aggregates with newly melted particles. The systematics of the aggregate morphologies supports the idea that the aggregates were formed in a single process. The alignment of

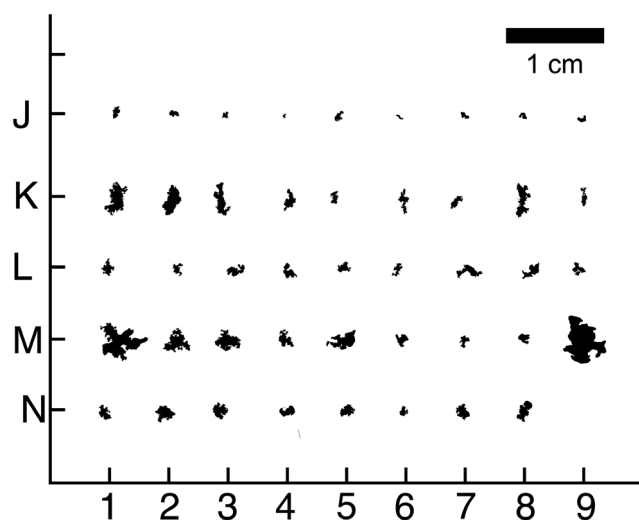


Fig. 12. Threshold image of different natural fractal inclusions in NWA 13656. Different types of inclusions are observed. J: Small inclusions consisting of only a few singles nodules. K: Elongated inclusions. L: Bent fractal inclusions. M: Fractal aggregates with four- and three-winged boomerang-shaped morphology. N: Inclusions with a massy center.

particles in the electric field between the electrodes prior to the arc discharges could have also influenced the formation of aggregates. The particle density between the electrodes (>80 vol%) was much higher than in the total sample chamber when the flash-heating event was triggered, and the particles could have immediately collided with their neighboring particles. This could have influenced the duration of aggregate formation which could have been much faster than our calculation of $\ll 0.5$ s.

Aggregates with a massy center could have formed from collisions of several molten droplets. The analysis of single melt droplets showed that the experiment was able to completely melt single particles (Koch, Spahr, Tkalec, et al., 2021). Some of these melt droplets could have collided with other completely molten grains, grains in the ductile state, or initial particles and formed massy aggregates. However, it is also possible that a fractal aggregate was partially melted by another heating event and formed a massy aggregate.

Furthermore, we could not find evidence for fragmentation of the aggregates. This could be due to several reasons. First, the aggregates were not directly hit by the ignition sparks. Further, aggregates could have been remelted to massy aggregates. Last, the collision energy between the moving particles and the aggregates could have been too low for fragmentation and collisions between two particles or aggregates which experienced melting resulted in sticking.

Relation to Early Solar System Processes

There are several similarities between the aggregates formed in our experiments and early solar system aggregates. In general, many of the aggregates formed in our experiment aboard the ISS resemble fluffy-type CAIs (MacPherson & Grossman, 1984), both in size and in their irregular-shaped morphologies. All different morphology types, for example, elongated aggregates, fractal and boomerang/bent aggregates, and massy aggregates can be found as morphologies of CAIs in a natural CV3 chondrite.

Furthermore, Zhang et al. (2021) performed CT analysis of refractory inclusions of five CV3 meteorites to study their three-dimensional morphology and found that among the six intact inclusions, three showed an elongated morphology with b/c ratios of 1.5–2.1 and two had a fractal and “swan-like” morphology. The mean b/c ratio of 2.1 ± 2 of the elongated aggregates formed in our experiment is similar to that observed for the natural refractory inclusions in the study of Zhang et al. (2021). Furthermore, the natural “swan-like” and bent inclusions shown in their study resemble aggregates formed in our experiment. The b/c ratio of the elongated, natural CAIs observed in NWA 13656 is also in accordance with the b/c ratio determined by Zhang et al. (2021) and the experimental outcomes of this study. For unknown reasons, aggregates and CAIs prefer a ratio of their longest to their shortest dimension in the range of 2. It is also notable that the largest aggregates formed in the experiment (Fig. 3h) and most of the largest fluffy-type CAIs in NWA 13656 (Figs. 11a–c) have the three-winged morphology.

The fluffy morphology of the formed aggregates resembles that of those formed from low velocity hit-and-stick collisions (Blum & Wurm, 2008) but were formed by a flash-heating event in the sample chamber. Earlier studies have already shown that CAI aggregation induced by turbulence produces CAIs with the same size distribution as CAIs in chondrites (Charnoz et al., 2015; Taillifet et al., 2014). The combination of the different analytical and theoretical studies discussed above together with our experiment implies that collisions of (flash-)heated particles can reproduce the typical fluffy-type CAIs. The aggregates formed in this experiment, even those that fused only superficially, remained stable over the whole duration of this experiment and during subsequent return transportation to Earth under gravity conditions, which should lead to friction and collisions with other particles, aggregates, and the sample chamber walls. In this regard we may note that CAIs observed in chondrites, even very fractal fluffy CAIs, have survived transport from their formation region to the chondrite

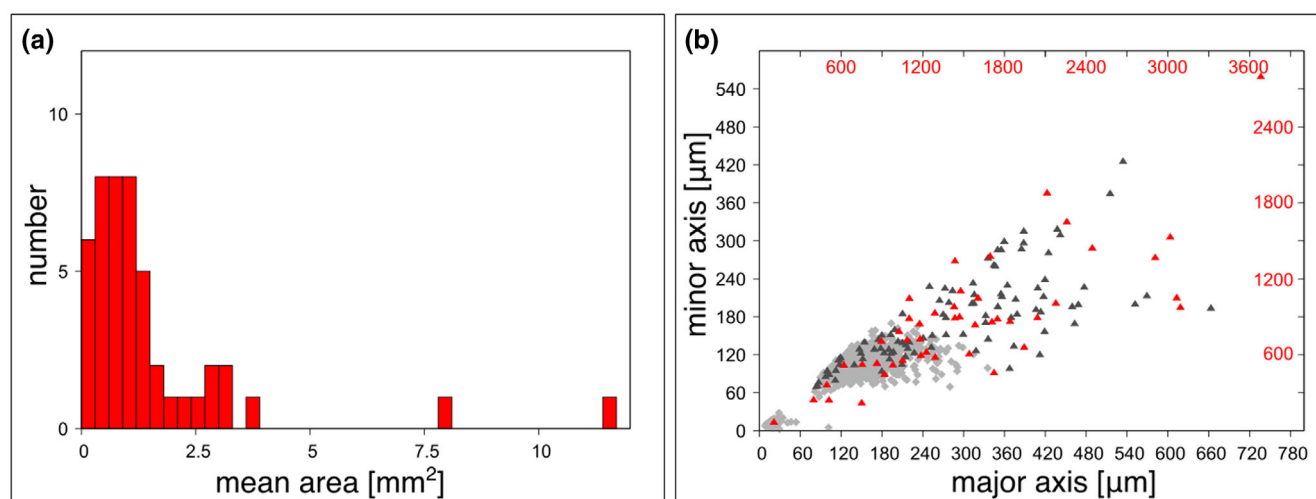


Fig. 13. Size analysis of irregular natural inclusions in NWA 13656. a) Histogram of the area size distribution. b) Major axis versus minor axis of the approximated ellipsoids (red) in comparison to the sizes of the experimental initial starting material (light gray) and the experimentally formed aggregates (dark gray). The sizes of the irregular natural inclusions in NWA 13656 are denoted by the red scale numbers since the natural CAIs have sizes of about a factor 5 larger than the experimentally formed aggregates (black-scale numbers). (Color figure can be viewed at wileyonlinelibrary.com.)

Table 2. Ratio of the longest (b) versus shortest (c) dimensions of different natural CAIs in NWA 13656.

No.	J1	J2	K1	K2	K3	K5	K7
b/c	1.9	1.8	2.6	2.1	3.5	2.0	2.7
No.	K8	K9	N4	N8			
b/c	3.4	3.2	2.1	1.8			

aggregation area by jets, turbulent diffusion, gravitational instabilities, or advection due to disk expansion (e.g., Cuzzi et al., 2003, 2005; Cuzzi & Hogan, 2003; Gounelle et al., 2001; Shu et al., 2001; Weidenschilling, 2003), which requires a certain amount of structural stability. Melting has already been proposed to influence the formation and stability of fluffy CAIs (Rubin, 2012). However, it has also been argued that the contact points of CAI nodules do not show evidence for melting or sintering (Russell & Howard, 2013). Yet we have shown that the interlocks between grains in the experiments have sometimes no visible melting zone. Furthermore, fluffy-type CAIs show evidence for melting next to unprocessed material (Russell & Howard, 2013), similar to the adjacency of molten and unprocessed material produced in the presented experiment. Consequently, a small amount of melting could have supplied the required stability for such fractal structures to have survived transportation and aggregation to and compaction within planetesimals.

Some particles of the experimentally formed aggregates are surrounded by igneous rims with a

thickness of approximately 20 μm . The thickness of the rims formed in our experiments is in the same size range as WLRs in natural CAIs (Bolser et al., 2016; Krot et al., 2017). The experimentally formed rims show a strong preferred orientation, which is similar to the orientation of the natural WLRs studied by Bolser et al. (2016) who explained the formation of WLRs by condensation from the nebula. However, Wark and Boynton (2001) suggested that flash-heating was involved in WLR formation and the recent study of Han et al. (2020) proposed that WLR formed by flash-heating followed by fast crystallization and gas solid reactions in a turbulent environment. Our results support the proposal that flash-heating could have induced or influenced WLR formation. However, the typically observed mineral sequence in WLRs could not be reproduced in our experiment due to the single phase used as starting material. Future experiments involving multiphase starting material could address whether flash-heating could also lead to multilayered multiminerall WLR analogues.

Disk- or bowl-shaped aggregates have also been observed in chondrites and interpreted as the results of shock flattening (Lorenz et al., 2019). Although we could only detect one aggregate that consists of a flat, molten disk (#F6), it indicates that aerodynamical forces, which occurred by the fast acceleration of the particles after the induced arc discharges, can also lead to a flattening of the molten droplet.

The studied massy aggregates formed experimentally resemble natural igneous CAIs; however,

they include many areas that did not experience melting. Aléon et al. (2013) reported an igneous CAI which shows evidence for partial melting, concluding that this CAI was the result of collisions of proto-CAIs which were partially molten. This interpretation is similar to our idea for the formation of massy aggregates in the experiment. It is also in agreement with the formation scenario for compound CAIs proposed by Ivanova et al. (2015). This aggregate type may represent a good example for CAI recycling during repeated events. Rubin (2012) suggested that type B CAIs formed from collisions of molten type A CAIs and that the difference during the formation of fluffy-type CAIs and this specific CAI is that the grains had different degrees of melting. This idea is in accordance with our interpretation of the formation of the fractal aggregates and massy aggregates formed during the experiment aboard the ISS.

In the experiment aboard the ISS, the different aggregates formed over a very short period of probably $\ll 0.5$ s with a very high cooling rate. The total particle density in our sample chamber is approximately 10^5 – 10^8 higher than that assumed for the natural CAI-forming region of the PPD (Zsom et al., 2010). In addition, the electric field prior to the flash-heating events caused an even higher particle density. However, it was proposed that the PPD had local enrichments of particles (Bischoff et al., 2017). These local higher particle densities in the PPD could be, for instance, the result of electrostatic or magnetic influences, which have been produced in this or some previous experiments (Love et al., 2014; Marshall et al., 2005; Nuth et al., 1994). The cooling rates of type B CAIs is another limiting factor in the formation of CAIs which are formed by flash-heating aggregates. They are generally thought to be much slower (approximately 50 K h^{-1} , e.g., MacPherson, Grossman, et al., 1984; MacPherson, Paque, et al., 1984) than the cooling rates determined for the particles in the experiments; however, a slower cooling rate would be required to form aggregates in a less dust-rich environment.

CONCLUSION

We carried out an experiment at long-term microgravity conditions aboard the ISS where freely floating particles were exposed to arc discharges. The experiment produced fused aggregates which resemble many specific morphological CAI characteristics reported in the literature, such as the fluffy-type CAI morphologies, igneous CAI textures with relict grains, disk-like CAIs, and WLRs. The fractal structures formed in the experiment are very stable which could explain why the fractal structures of fluffy-type CAIs

survived transportation to the chondrite accretion region and chondrite parent body formation. The high acceleration of particles would lead to disk- and bowl-shaped CAIs. Collisions of CAI nodules with different degrees of melting can form igneous and compound CAIs. In summary, these results imply that periodically repeated local (flash-)heating events with subsequent aggregation of particles could have been involved in CAI formation after their condensation.

Acknowledgments—This project was realized with the help of A.A. Beck and D. Mederos Leber. We thank the Hackerspace Ffm e. V., especially S. Fujita and J. Kerscher, R. Haseitl, and S. Matthies for help with technical implementation and software development. We thank J. Weppeler and the German Aerospace Center DLR for taking care of the organization of this project. We thank NanoRacks LLC and DreamUp for the payload opportunity. We also thank the astronauts aboard the ISS under the commandant of A. Gerst for the implementation of the experiment. We are grateful for financial support provided by the Dr. Rolf M. Schwiete Stiftung, the German Aerospace Center DLR, NanoRacks LLC, DreamUp, Biovia, the BmWi (50JR1704) and DFG (BR2015/35-1; Wi1232/44-1), Nordlicht GmbH, and ZEISS. We acknowledge DESY (Hamburg, Germany), a member of the Helmholtz Association HGF, for the provision of experimental facilities. Parts of this research were carried out at PETRA III. BW is grateful for support through the BIOVIA Science Ambassador program. The manuscript benefited from comments from M. Komatsu and J. Nuth.

Data Availability Statement—Data available on request from the authors.

Editorial Handling—Dr. Michael Zolensky

REFERENCES

- Aléon, J., Marin-Carbonne, J., Taillifet, E., Mckeegan, K., Charnoz, S., and Baillie, K. 2013. Igneous CAI Growth by Coagulation and Partial Melting of Smaller Proto-CAIs: Insights from a Compact Type A CAI and from Modeling (Abstract #2530). 44th Lunar and Planetary Science Conference. CD-ROM.
- Anthony, J. W., Bideaux, R. A., Bladh, K. W., and Nichols, M. C. (Eds.). 2018. *Handbook of Mineralogy*. Chantilly: Mineralogical Society of America.
- Beitz, E., Guettler, C., Weidling, R., and Blum, J. 2012. Free Collisions in a Microgravity Many-Particle Experiment-II: The Collision Dynamics of Dust-Coated Chondrules. *Icarus* 218: 701–6.

- Bischoff, A., Wurm, G., Chaussidon, M., Horstmann, M., Metzler, K., Weyrauch, M., and Weinauer, J. 2017. The Allende Multicomponent Chondrule (ACC)—Chondrule Formation in a Local Super-Dense Region of the Early Solar System. *Meteoritics & Planetary Science* 52: 906–24.
- Bland, P. A., Howard, L. E., Prior, D. J., Wheeler, J., Hough, R. M., and Dyl, K. A. 2011. Earliest Rock Fabric Formed in the Solar System Preserved in a Chondrule Rim. *Nature Geoscience* 4: 244–7.
- Blander, M., and Fuchs, L. H. 1975. Calcium-Aluminum-Rich Inclusions in the Allende Meteorite: Evidence for a Liquid Origin. *Geochimica et Cosmochimica Acta* 39: 1605–19.
- Blum, J. 2010. Astrophysical Microgravity Experiments with Dust Particles. *Microgravity Science and Technology* 22: 517–27.
- Blum, J., and Wurm, G. 2008. The Growth Mechanisms of Macroscopic Bodies in Protoplanetary Disks. *Annual Review of Astronomy and Astrophysics* 46: 21–56.
- Blum, J., Wurm, G., Kempf, S., Poppe, T., Klahr, H., Kozasa, T., Rott, M. et al. 2000. Growth and Form of Planetary Seedlings: Results from a Microgravity Aggregation Experiment. *Physical Review Letters* 85: 2426–9.
- Blum, J., Wurm, G., Poppe, T., Kempf, S., and Kozasa, T. 2002. First Results from the Cosmic Dust Aggregation Experiment CODAG. *Advances in Space Research* 29: 497–503.
- Bolser, D., Zega, T. J., Asaduzzaman, A., Bringuier, S., Simon, S. B., Grossman, L., Thompson, M. S., and Domanik, K. J. 2016. Microstructural analysis of Wark-Lovering Rims in the Allende and Axtell CV3 Chondrites: Implications for High-Temperature Nebular Processes. *Meteoritics & Planetary Science* 51: 743–56.
- Bowen, N. L., and Schairer, J. F. 1925. The System MgO-FeO-SiO₂. *American Journal of Science* 29: 151–217.
- Brauer, F., Dullemond, C. P., and Henning, T. 2007. Coagulation, Fragmentation and Radial Motion of Solid Particles in Protoplanetary Disks. *Astronomy & Astrophysics* 480: 859–77.
- Charnoz, S., Aléon, J., Chaumard, N., Baillie, K., and Taillifet, E. 2015. Growth of Calcium–Aluminum-Rich Inclusions by Coagulation and Fragmentation in a Turbulent Protoplanetary Disk: Observations and Simulations. *Icarus* 252: 440–53.
- Charnoz, S., and Taillifet, E. 2012. A Method for Coupling Dynamical and Collisional Evolution of Dust in Circumstellar Disks: The Effect of a Dead Zone. *The Astrophysical Journal* 753: 119.
- Ciesla, F. J., Lauretta, D. S., and Hood, L. L. 2004. The Frequency of Compound Chondrules and Implications for Chondrule Formation. *Meteoritics & Planetary Science* 39: 531–44.
- Connelly, J. N., Bizzarro, M., Krot, A. N., Nordlund, A., Wielandt, D., and Ivanova, M. A. 2012. The Absolute Chronology and Thermal Processing of Solids in the Solar Protoplanetary Disk. *Science* 338: 651–5.
- Connolly Jr., H. C., and Libourel, G. E. 2005. *Experimental Constraints on Chondrule Formation*. Chondrites and the Protoplanetary Disk, ASP Conference Series, 341, 286. San Francisco: Astronomical Society of the Pacific.
- Cuzzi, J., Ciesla, F., Petaev, M., Krot, A., Scott, E., and Weidenschilling, S. 2005. Nebula Evolution of Thermally Processed Solids: Reconciling Models and Meteorites. ASP Conference Series 341, 732–73. San Francisco: Astronomical Society of the Pacific.
- Cuzzi, J. N., Davis, S. S., and Dobrovolskis, A. R. 2003. Blowing in the Wind. II. Creation and Redistribution of Refractory Inclusions in a Turbulent Protoplanetary Nebula. *Icarus* 166: 385–402.
- Cuzzi, J. N., and Hogan, R. C. 2003. Blowing in the Wind: I. Velocities of Chondrule-Sized Particles in a Turbulent Protoplanetary Nebula. *Icarus* 164: 127–38.
- Dominik, C., Blum, J., Cuzzi, J., and Wurm, G. 2006. Growth of Dust as the Initial Step Toward Planet Formation. In *Protostars and Planets V*. Tucson: University of Arizona Press.
- Gounelle, M., Shu, F. H., Shang, H., Glassgold, A. E., Rehm, K. E., and Lee, T. 2001. Extinct Radioactivities and Protosolar Cosmic Rays: Self-Shielding and Light Elements. *The Astrophysical Journal* 548: 1051–70.
- Han, J., and Brearley, A. J. 2015. Microstructural Evidence for Complex Formation Histories of Amoeboid Olivine Aggregates from the ALHA77307 CO3.0 Chondrite. *Meteoritics & Planetary Science* 50: 904–25.
- Han, J., Keller, L. P., Liu, M.-C., Needham, A. W., Hertwig, A. T., Messenger, S., and Simon, J. I. 2020. A Coordinated Microstructural and Isotopic Study of a Wark-Lovering Rim on a Vigarano CAI. *Geochimica et Cosmochimica Acta* 269: 639–60.
- Ivanova, M. A., Kononkova, N. N., Krot, A. N., Greenwood, R. C., Franchi, I. A., Verchovsky, A. B., Trieloff, M., Korochantseva, E. V., and Brandstätter F. 2008. The Isheyevo Meteorite: Mineralogy, Petrology, Bulk Chemistry, Oxygen, Nitrogen, Carbon Isotopic Compositions, and 40Ar-39Ar ages. *Meteoritics & Planetary Science* 43: 915–40.
- Ivanova, M. A., Lorenz, C. A., Krot, A. N., and MacPherson, G. J. 2015. A Compound Ca-, Al-Rich Inclusion from CV3 Chondrite Northwest Africa 3118: Implications for Understanding Processes During CAI Formation. *Meteoritics & Planetary Science* 50: 1512–28.
- Kita, N. T., Yin, Q.-Z., MacPherson, G. J., Ushikubo, T., Jacobsen, B., Nagashima, K., Kurahashi, E., Krot, A. N., and Jacobsen, S. B. 2013. ²⁶Al-²⁶Mg Isotope Systematics of the First Solids in the Early Solar System. *Meteoritics & Planetary Science* 48: 1383–400.
- Koch, T. E., Spahr, D., Merges, D., Winkler, B., and Brenker, F. E. 2021. Mg₂SiO₄ Particle Aggregation Aboard the ISS—Influence of Electric Fields on Aggregation Behavior, Particle Velocity and Shape-Preferred Orientation. *Astronomy & Astrophysics* 653: A1.
- Koch, T. E., Spahr, D., Tkalcic, B. J., Lindne, M., Merges, D., Wilde, F., Winkler, B., and Brenker, F. E. 2021. Formation of Chondrule Analogues Aboard the International Space Station. *Meteoritics & Planetary Science* 56: 1669–84.
- Komatsu, M., Krot, A. N., Petaev, M. I., Ulyanov, A. A., Keil, K., and Miyamoto, M. 2001. Mineralogy and Petrography of Amoeboid Olivine Aggregates from the Reduced CV3 Chondrites Efremovka, Leoville and Vigarano: Products of Nebular Condensation, Accretion and Annealing. *Meteoritics & Planetary Science* 36: 629–41.
- Komatsu, M., Mikouchi, T., and Miyamoto, M. 2009. High-Temperature Annealing of Amoeboid Olivine Aggregates: Heating Experiments on Olivine-Anorthite Mixtures. *Polar Science* 3: 31–55.
- Kozub, D., Khmelik, V., Shapoval, J., Chentsov, V., Yatsenko, S., Litovchenko, B., and Starikh, V. 2018.

- Helicon Focus 7.0.2 Pro. <https://www.heliconsoft.com/heliconsoft-products/helicon-focus/>.
- Krot, A. N. 2019. Refractory Inclusions in Carbonaceous Chondrites: Records of Early Solar System Processes. *Meteoritics & Planetary Science* 54: 1647–91.
- Krot, A. N., Amelin, Y., Bland, P., Ciesla, F. J., Connelly, J., Davis, A. M., Huss, G. R. et al. 2009. Origin and Chronology of Chondritic Components: A Review. *Geochimica et Cosmochimica Acta* 73: 4963–97.
- Krot, A. N., Nagashima, K., van Kooten, E. M. M., and Bizzarro, M. 2017. High-Temperature Rims Around Calcium–Aluminum-Rich Inclusions from the CR, CB and CH Carbonaceous Chondrites. *Geochimica et Cosmochimica Acta* 201: 155–84.
- Krot, A. N., Petaev, M. I., Russell, S. S., Itoh, S., Fagan, T. J., Yurimoto, H., Chizmadia, L. et al. 2004. Amoeboid Olivine Aggregates and Related Objects in Carbonaceous Chondrites: Records of Nebular and Asteroid Processes. *Chemie der Erde—Geochemistry* 64: 185–239.
- Krot, A. N., Petaev, M. I., and Yurimoto, H. 2004. Amoeboid Olivine Aggregates with Low-Ca Pyroxenes: A Genetic Link Between Refractory Inclusions and Chondrules? *Geochimica et Cosmochimica Acta* 68: 1923–41.
- Liffman, K., Cuello, N., and Paterson, D. A. 2016. A Unified Framework for Producing CAI Melting, Wark–Lovering Rims and Bowl-Shaped CAIs. *Monthly Notices of the Royal Astronomical Society* 462: 1137–63. <https://doi.org/10.1093/mnras/stw1563>
- Lorenz, C., Ivanova, M., Krot, A., and Shuvalov, V. 2019. Formation of Disk- and Bowl-Shaped Igneous Ca, Al-Rich Inclusions: Constraints from their Morphology, Textures, Mineralogy and Modelling. *Geochemistry* 79: 125523.
- Love, S. G., Pettit, D. R., and Messenger, S. R. 2014. Particle Aggregation in Microgravity: Informal Experiments on the International Space Station. *Meteoritics & Planetary Science* 49: 732–9.
- MacPherson, G. J., and Grossman L. 1984. “Fluffy” Type A Ca-, Al-Rich Inclusions in the Allende Meteorite. *Geochimica et Cosmochimica Acta* 48: 29–46.
- MacPherson, G. J., Grossman, L., Allen, J. M., and Beckett, J. R. 1982. Origin of Rims on Coarse-Grained Inclusions in the Allende Meteorite. 12th Lunar and Planetary Science Conference. pp. 1079–91.
- MacPherson, G. J., Grossman, L., Hashimoto, A., Bar-Matthews, M., and Tanaka, T. 1984. Petrographic Studies of Refractory Inclusions from the Murchison Meteorite. *Journal of Geophysical Research: Solid Earth* 89: C299–312.
- MacPherson, G. J., Paque, J. M., Stolper, E., and Grossman, L. 1984. The Origin and Significance of Reverse Zoning in Melilite from Allende Type B Inclusions. *The Journal of Geology* 92: 289–305.
- Marrocchi, Y., Villeneuve, J., Jacquet, E., Piralla, M., and Chaussidon, M. 2019. Rapid Condensation of the First Solar System Solids. *Proceedings of the National Academy of Sciences* 116: 23461–6.
- Marshall, J. R., Sauke, T. B., and Cuzzi, J. N. 2005. Microgravity Studies of Aggregation in Particulate Clouds. *Geophysical Research Letters* 32: L11202.
- Moosmann, J., Ershov, A., Weinhardt, V., Baumbach, T., Prasad, M. S., LaBonne, C., Xiao, X., Kashef, J., and Hofmann, R. 2014. Time-Lapse X-Ray Phase-Contrast Microtomography for In Vivo Imaging and Analysis of Morphogenesis. *Nature Protocols* 9: 294–304.
- Morris, M. A., and Desch, S. J. 2010. Thermal Histories of Chondrules in Solar Nebula Shocks. *The Astrophysical Journal* 722: 1474–94.
- Nakagawa, Y., Nakazawa, K., and Hayashi, C. 1981. Growth and Sedimentation of Dust Grains in the Primordial Solar Nebula. *Icarus* 45: 517–28.
- NIST. 2020. NIST: National Institute of Standards and Technology. Solid Phase Heat Capacity. <https://webbook.nist.gov/cgi/cbook.cgi?ID=C10034943&Units=SI&Mask=2&Type=JANAFS&Plot=on#JANAFS> (6 June 2020).
- Nuth, J. N., Berg, O., Faris, J., and Wasiliewski, P. 1994. Magnetically Enhanced Coagulation of Very Small Iron Grains. *Icarus* 107: 155–63.
- Ogurreck, M., Wilde, F., Herzen, J., Beckmann, F., Nazmov, V., Mohr, J., Haibel, A., Müller, M., and Schreyer, A. 2013. The Nanotomography Endstation at the PETRA III Imaging Beamline. *Journal of Physics: Conference Series* 425: 182002.
- Rubin, A. 2012. A New Model for the Origin of Type-B and Fluffy Type-A CAIs: Analogies to Remelted Compound Chondrules. *Meteoritics & Planetary Science* 47: 1062–74.
- Rueden, C. T., Schindelin, J., Hiner, M. C., DeZonia, B. E., Walter, A. E., Arena, E. T., and Eliceiri, K. W. 2017. ImageJ2: ImageJ for the Next Generation of Scientific Image Data. *BMC Bioinformatics* 18: 529.
- Russell, S. S., and Howard, L. 2013. The Texture of a Fine-Grained Calcium–Aluminium-Rich Inclusion (CAI) in Three Dimensions and Implications for Early Solar System Condensation. *Geochimica et Cosmochimica Acta* 116: 52–62.
- Shu, F. H., Shang, H., Gounelle, M., Glassgold, A. E., and Lee, T. 2001. The Origin of Chondrules and Refractory Inclusions in Chondritic Meteorites. *The Astrophysical Journal* 548: 1029–50.
- Spahr, D., Koch, T. E., Merges, D., Beck, A. A., Bohlender, B., Carlsson, J. M., Christ, O. et al. 2020. A Chondrule Formation Experiment Aboard the ISS: Experimental Set-Up and Test Experiments. *Icarus* 350: 113898.
- Steinpilz, T., Joeris, K., Jungmann, F., Wolf, D., Brendel, L., Teiser, J., Shinbrot, T., and Wurm, G. 2020. Electrical Charging Overcomes the Bouncing Barrier in Planet Formation. *Nature Physics* 16: 225–9.
- Sugiura, N., Petaev, M. I., Kimura, M., Miyazaki, A., and Hiyagon, H. 2009. Nebular History of Amoeboid Olivine Aggregates. *Meteoritics & Planetary Science* 44: 559–72.
- Taillifet, E., Baillié, K., Charnoz, S., and Aléon, J. 2014. Origin of Refractory Inclusion Diversity by Turbulent Transport in the Inner Solar Nebula (Abstract #2086). 45th Lunar and Planetary Science Conference. CD-ROM.
- Tkalcec, B. J., Golabek, G. J., and Brenker, F. E. 2013. Solid-State Plastic Deformation in the Dynamic Interior of a Differentiated Asteroid. *Nature Geoscience* 6: 93–7.
- Wark, D., and Boynton, W. V. 2001. The Formation of Rims on Calcium–Aluminum-Rich Inclusions: Step I—Flash Heating. *Meteoritics & Planetary Science* 36: 1135–66.
- Wark, D. A., and Lovering, J. F. 1977. Marker Events in the Early Evolution of the Solar System: Evidence from Rims on Ca–Al-Rich Inclusions in Carbonaceous Chondrites. Proceedings, 8th Lunar Science Conference. pp. 95–112.
- Weidenschilling, S. J. 2003. Radial Drift of Particles in the Solar Nebula: Implications for Planetesimal Formation. *Icarus* 165: 438–42.

- Wilde, F., Ogurreck, M., Greving, I., Hammel, J. U., Beckmann, F., Hipp, A., Lottermoser, L. et al. 2016. Micro-CT at the Imaging Beamline P05 at PETRA III. *AIP Conference Proceedings* 1741: 30035.
- Wurm, G., and Blum, J. 1998. Experiments on Preplanetary Dust Aggregation. *Icarus* 132: 125–36.
- Zhang, M., Clark, B., King, A. J., Russell, S. S., and Lin, Y. 2021. Shape and Porosity of Refractory Inclusions in CV3 Chondrites: A Micro-Computed Tomography (μ CT) Study. *Meteoritics & Planetary Science* 56: 500–14.
- Zsom, A., Ormel, C. W., Güttler, C., Blum, J., and Dullemond, C. P. 2010. The Outcome of Protoplanetary Dust Growth: Pebbles, Boulders, or Planetesimals? II. Introducing the Bouncing Barrier. *Astronomy & Astrophysics* 513: A57.
-